IOP Publishing | International Atomic Energy Agency Nuclear Fusion

Nucl. Fusion **59** (2019) 066018 (7pp) https://doi.org/10.1088/1741-4326/ab1578

Cross-separatrix simulations of turbulent transport in the field-reversed configuration

C.K. Lau[1], D.P. Fulton[1], J. Bao[2], Z. Lin[2], T. Tajima[1,2], L. Schmitz[1,3], S. Dettrick[1] and the TAE Team[1]

[1] TAE Technologies, Foothill Ranch, CA, United States of America
[2] Department of Physics and Astronomy, University of California, Irvine, CA, United States of America
[3] Department of Physics and Astronomy, University of California, Los Angeles, CA, United States of America

E-mail: clau@tae.com

Received 3 January 2019, revised 28 February 2019
Accepted for publication 2 April 2019
Published 2 May 2019

Abstract

Recent local simulations of the field-reversed configuration (FRC) have reported drift-wave stability in the core and instability in the scrape-off layer (SOL). However, experimental measurements indicate the existence of fluctuations in both FRC core and SOL, with much lower amplitude fluctuations measured in the core. With the updated cross-separatrix capabilities of the simulation code used in this paper, nonlinear turbulence simulations find that linear instabilities grow in the SOL, generating fluctuations which spread from SOL to core. After saturation of the linear instabilities, a balance of the inward spread and local damping in the core is achieved. The steady state toroidal wavenumber spectrum shows lower amplitude core fluctuations and larger SOL fluctuations with amplitude decreasing towards shorter wavelengths, which are consistent with experimental measurements.

Keywords: field-reversed configuration, turbulence, particle-in-cell, cross-separatrix

(Some figures may appear in colour only in the online journal)

1. Introduction

An ideal field-reversed configuration (FRC) is an elongated prolate compact toroid (CT) with purely poloidal magnetic fields, consisting of two regions separated by a separatrix: an inner, closed field-line core region and an outer, open field-line scrape-off layer (SOL) region [1, 2]. Research interest in the FRC has persisted due to potential reactor benefits [1]: β (the ratio of plasma pressure to magnetic energy density) near unity suggests cheaper magnetic energy costs than low β approaches such as the tokamak [2]; compact shape simplifies construction of the device hull and external magnetic field coils [3]; on-axis SOL which may be connected to the divertor arbitrarily far from the FRC core; and [4] the lack of toroidal magnetic fields radically changes the magnetic topology and the consequential stability of the plasma [3, 4].

In recent years at the C-2/C-2U FRC experiment, experimental progress by TAE Technologies, Inc. (TAE) led to successful reduction of major macro-instabilities (rotational $n = 2$, wobble, and tilt $n = 1$ modes [1], where n is the toroidal mode number). By doing so, FRC plasma sustainment times have been increased to the order of several milliseconds [5, 6, 7], and this confinement approach is now in transport-limited regimes [7, 8]. After the necessary stabilization of the macro-instabilities, the next essential step to a viable FRC fusion reactor is to understand the transport processes within FRC plasmas.

Experimental measurements of density fluctuations using Doppler Backscattering (DBS [9]) in the C-2/C-2U FRC device have shown that fluctuations of the core and SOL of FRC plasmas exhibit distinct qualities. In the SOL, the fluctuation spectrum is exponentially decreasing towards electron-scale wavelengths and highest in amplitude towards ion-scale wavelengths. In the core, the fluctuation spectrum is overall lower in amplitude with a dip in the ion-scale wavelengths and a slight peak in electron-scale lengths, which further decrease towards even shorter lengths [10].

Local linear simulations [11, 12, 13] using the gyrokinetic toroidal code (GTC) [14] have found qualitatively similar results. The SOL is linearly unstable for a wide range of length scales and varying pressure gradients. In addition, the critical instability thresholds found for the SOL in the local linear

simulations are comparable to the experimentally measured fluctuation threshold. On the other hand, the core is robustly stable due to the stabilizing FRC traits of short field-line connection lengths, radially increasing magnetic field strength, and the large finite Larmor radius (FLR) [15] of ions.

While there is also ongoing work towards understanding FRC transport with hybrid kinetic/fluid transport codes, namely Q1D [16] and Q2D [17], the present work is the first global nonlinear gyrokinetic transport study of turbulence in the FRC. We expand on the past linear physics simulations mentioned above [13] to push into the nonlinear kinetic simulations required for understanding turbulence-driven transport.

In this work, global linear simulations also find agreement with previous local linear simulations on core stability and SOL instability. Simulations of a single toroidal mode have demonstrated fluctuations spreading from the SOL region into the FRC core. Simulations of multiple toroidal modes, confined only to the SOL, show an inverse cascade in the fluctuation spectrum due to mode-mode coupling. Finally, global simulations of multiple toroidal modes including both the SOL and core regions find that the combined features of the inverse cascade and turbulence spreading lead to a fluctuation spectrum that is qualitatively comparable to the aforementioned experimental results of Schmitz *et al* [10]

2. Simulation model

In this paper, simulations have been conducted with the turbulence code, ANC, in a C-2/C-2U-like magnetic geometry. ANC is a global particle-in-cell (PIC) code [18, 19], suitable for simulation of electrostatic drift-wave turbulence. In this work, electrostatic perturbative δf simulations [20–24] are confined to a nonlocal domain spanning the confinement vessel region. The electrostatic Poisson equation is simplified by the Padé approximation

$$-\tilde{\nabla}_{\perp}^{2}\hat{\phi} = (1 - \tilde{\nabla}_{\perp}^{2})\delta\hat{n}$$

(where the $\hat{\phi}$ is the normalized electrostatic potential, $\delta\hat{n}$ is the normalized perturbed charge density, and $\tilde{\nabla}_{\perp}^{2}$ is the normalized Laplacian) and solved using the Portable, Extensible Toolkit for Scientific Computation (PETSc) via the Krylov method. Thermal ions are modeled with gyrokinetic deuterium, time-advanced by Runge–Kutta 4th order, and electrons are modeled with an adiabatic response $\left(\frac{\delta n_e}{n_0} \approx \frac{e\phi}{T_e}\right)$, without collisions. Although neutral beam injection is used in the experiments to stabilize macro-instabilities and sustain the FRC, beam ions are not included in the current simulations. To preserve gyrokinetic validity, the magnetic field null region is excluded as shown in figure 1. Perturbed quantities near the radial boundaries are smoothly set to zero to reduce boundary effects. In this simulation domain, periodic boundaries are used in the axial (Z) directions, neglecting parallel outflow effects. Details about the specifics of the code, including algorithm and benchmarks, will be published in a future paper.

These simulations are initialized with an FRC equilibrium [25] with density and ion temperature gradients and flat electron temperature corresponding to table 1, with the distance from the machine axis to the separatrix at the outer midplane is $R_s = 38\,\text{cm}$. Because ANC uses the perturbative δf model, these equilibrium profiles do not evolve within the simulation. The use of the flat electron temperature and the adiabatic electron response serve to simplify the physics model as an initial step for the recently updated simulation model of this paper, which extends the simulation domain to include both the core and SOL regions. In upcoming work, the electron model will be extended to drift-kinetic electrons with a more realistic electron temperature profile.

In section 3, the simulation domain extends from the SOL to the core but only allows for a single toroidal mode ($n = 20$ is shown). In section 4, the simulation domain is confined to the SOL but allows for multiple toroidal modes ($n = \{5, 10, ... ,75, 80\}$). In section 5, the simulation domain extends from the SOL to the core and allows for multiple toroidal modes ($n = \{0, 5, 10, ..., 75\}$). The factors of 5 in the toroidal modes selected in sections 4 and 5 are due to the use of toroidal symmetry for numerical reduction of the toroidal domain into a wedge 1/5 the size of the full toroidal domain. Simulations of a smaller toroidal wedge 1/10 the size of the full torus yield similar results in saturation levels and toroidal spectra.

3. Fluctuations spreading from SOL to core

With the equilibrium and model as described in section 2, linear simulations of a single toroidal mode show exponential growth of instability in the SOL with toroidal propagation in the ion diamagnetic direction. Comparison with local linear theory indicates that this is a slab-like ion temperature gradient (ITG) drift-wave instability [19].

In previous local, linear simulations [13], the SOL was found to be unstable while the core was stable. A variety of effects were studied, and core stability was found to be due to the stabilizing FRC traits of [1] short electron transit length [2], radially increasing magnetic field on the outboard side, and [3] strong FLR effects due to weak magnetic field. In the initial linear simulations of this section, nonlocal effects were numerically removed, effectively localizing the physics of the simulations. Consistent with past local simulations, there is no mode growth in the core due to the stabilizing effects mentioned, although the short electron transit effect is artificially enhanced by only using the electron adiabatic response in our equations.

In contrast to the past work, realistic nonlocal physics can be included through the Laplacian in the Poisson equation and through the gyroaveraging in the particle model. With these nonlocal effects included, drift-surfaces of different poloidal flux labels ψ are physically coupled. This introduces a radial wavenumber k_ψ into the wave dispersion, allowing for radial wave propagation such that a radial eigenmode structure forms across the SOL and core. Despite the physical coupling, in linear simulations, the amplitude of the eigenmode structure in the core is lower than in the SOL by more than

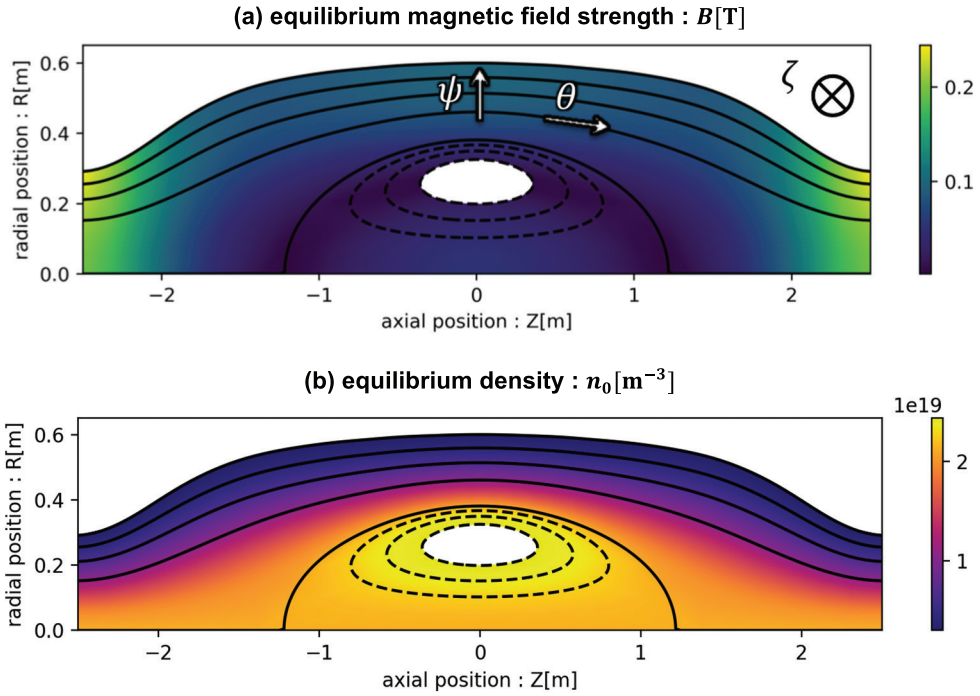

Figure 1. (*a*) The magnitude of the equilibrium FRC magnetic field is shown as the color of the filled contour plot, and (*b*) the equilibrium density is shown as the color of the filled contour plot. Note that the magnetic field null region ($Z = 0$ m, $R \sim 0.25$ m) is not included in the simulation domain. The black contour lines correspond to drift-surfaces corresponding to different poloidal flux contours. The distance from the machine axis to the separatrix (the last solid line before the dashed lines corresponding to negative flux) at the outer midplane is $R_s = 38$ cm. The magnetic coordinate system referred to within the paper is also shown: $\hat{\psi}$ is the direction of radially increasing poloidal flux, $\hat{\theta}$ is the direction along the magnetic field-lines, ie. poloidal, and $\hat{\zeta}$ is the direction about the machine axis, ie. azimuthal or toroidal.

Table 1. Simulation parameters in units of cm at $R = 53$ cm (the distance from the machine axis) where SOL linear instability is found, where $L_{T,i}$ and $L_{T,e}$ are the ion and electron temperature scale lengths, L_n is the density scale length, and ρ_i and ρ_e are the ion and electron gyroradii.

$L_{T,i}$	$L_{T,e}$	L_n	ρ_i	ρ_e
5.36	∞	10.7	1.1	0.022

a factor of 100. When nonlinear $\delta\vec{E} \times \vec{B}$ effects are included in the simulations, ie. when simulation marker particles are subjected to $\delta\vec{E} \times \vec{B}$ drift due to the self-consistent fields that arise, the mode saturates at a SOL mode amplitude of about $e\phi/T_e \sim 5 \times 10^{-2}$ as seen in figure 2 at $t \approx 1.25$ ms. On the other hand, the saturation level in the core is about a factor of ten lower than in the SOL due to a balance of the inward spread and the local damping in the core region, consistent with experimental measurements showing lower fluctuation amplitudes in the FRC core [10].

This process can be seen in the bottom panel of figure 2 which shows the mode amplitude in the core and SOL: initially, the unstable mode first grows in the SOL but has not started to grow in the core; at $t \approx 0.5$ ms, the radial eigenmode has formed such that the mode amplitude in the core is growing at the same growth-rate. This whole process is also shown in the top panel of figure 2, which shows the mode growing in the SOL first before spreading into the core.

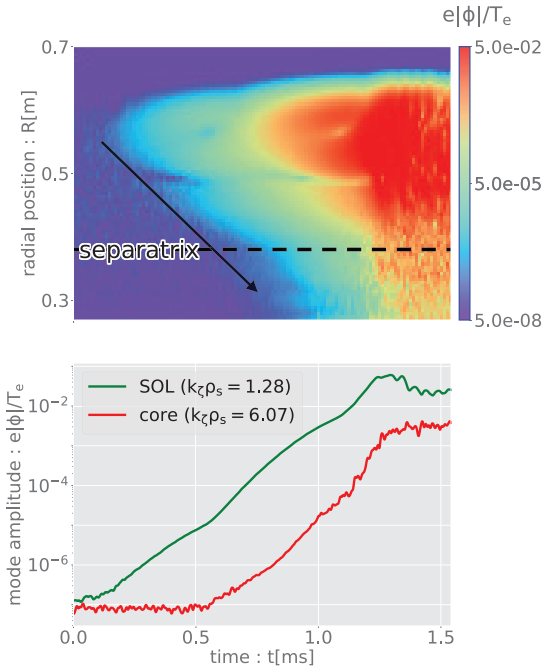

Figure 2. (TOP) The magnitude of the electrostatic potential along the outer midplane, $\phi(R, Z = 0, t)$, is shown with the colorbar following a logarithmic scale, and the dashed line indicates the location of the separatrix. (Bottom) Line-outs from the top plot corresponding to the SOL and core regions are shown in green and red, respectively.

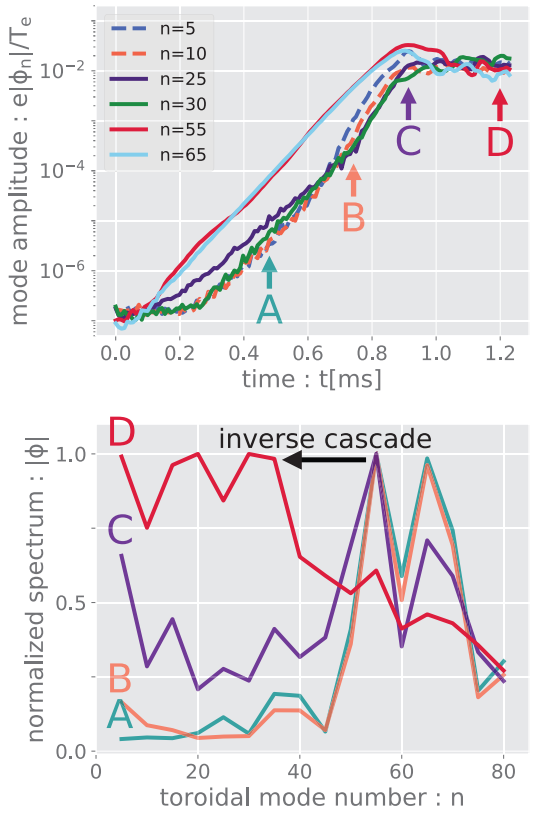

Figure 3. (Top) The magnitude of the electrostatic potential is shown for several toroidal modes (only a subset of the modes in the simulation are shown for clarity). (Bottom) The toroidal modenumber spectra corresponding to times marked in the top plot are shown. Here, the spectra are normalized by the maximum value for qualitative comparison for different times. For the subset of toroidal mode numbers, the mode numbers $n = \{5, 10, 25, 30, 55, 65\}$ are equivalent to wavenumbers $k_\zeta \rho_s = \{0.32, 0.64, 1.6, 1.9, 3.5, 4.2\}$ in the SOL.

4. Inverse spectral cascade in the SOL

To focus on the characteristics of SOL turbulence, the domain of simulations in this section is limited to the SOL. Multiple toroidal modes can interact nonlinearly, resulting in a turbulence state. Simulations of this section allow for the inclusion of multiple toroidal modes ($n = \{5, 10, ..., 75, 80\}$) where the toroidal modes $n = \{5, 10, 15\}$ were previously found to be linearly stable or damped modes.

Here, the unstable modes saturate at $e\phi/T_e \sim O(10^{-2})$ as seen in the top panel of figure 3. The saturation levels of these multiple-mode simulations are comparable to the single-mode simulations. Since the main saturation mechanism is unchanged despite the restriction in simulation domain, the physics of these multiple-mode simulations confined to just the SOL region remain valid for FRC simulations which include the core region.

Initially, the largest and fastest growing modes of this simulation are $n = 55$ and $n = 65$. In these simulations, different modes can couple to each other through the beating of two waves to excite a third, when wave matching conditions ($\vec{k_1} + \vec{k_2} = \vec{k_3}$, $\omega_1 + \omega_2 = \omega_3$) are met. Because lower toroidal mode numbers can more easily satisfy these matching conditions, an inverse toroidal spectral cascade occurs from the higher amplitude shorter wavelength modes to the linearly stable longer wavelength modes.

This process can be seen dynamically in the top panel of figure 3 which shows a subset of the simulated modes: at (A), the highest amplitudes belong to the high-n modes; at (B), the linearly stable low-n modes (dashed lines) have overtaken some of mid-n modes and nonlinear coupling is suggested by the growth-rates which are roughly twice the value of the linearly unstable modes; at (C), the modes are saturating but the inverse cascade continues and the high-n modes are beginning to lower in amplitude; and at (D), some time after saturation, the high-n modes are the lowest in amplitude while the low-n modes are the highest. Snapshots of the toroidal wavenumber spectrum corresponding to these four times are also shown in the bottom panel of figure 3. Overall, this inverse cascade corresponds to a change from an average wavelength of $\langle k_\zeta \rho_s \rangle \sim 3$ during the linearly growing phase, (A) and (B), to an average wavelength of $\langle k_\zeta \rho_s \rangle \sim$ 1.9 after the nonlinear cascade, (D).

5. Global turbulence from SOL to core

In this section, the simulations of multiple toroidal modes ($n = \{0, 5, 10, ..., 75\}$) now span both the SOL and core regions. Note that the $n = 0$ mode is also included, allowing for an additional available channel for mode coupling. As in section 3, with the inclusion of the core region, instability only grows in the SOL, but fluctuations spread into the core. In addition, with multiple toroidal modes as in section 4, energy cascades from the unstable shorter wavelength modes to the longer wavelength modes. Together, these two processes shape the toroidal spectra of the FRC core and SOL as shown in figure 5.

The electrostatic potential mode structures, viewed along the machine axis at the center of the confinement vessel and viewed from afar, from times corresponding to linear growth and nonlinear saturation are shown in figure 4. The purple shell corresponds to the separatrix, and the grey ring is the region near the null point, which is not included within the simulation domain due to gyrokinetic validity. (Note that the inner core region is connected to the outer core region through the parallel direction itself, as more easily seen from the other viewpoint.)

Consistent with the simulations of sections 3 and 4, fluctuations are lower in amplitude in the core and an inverse cascade in the SOL is observed. The inverse cascade can be graphically seen from the change in the short wavelength mode structures in figures 4(*a*) and (*b*) to the larger scale turbulent eddies in figures 4(*c*) and (*d*). Due to turbulence spreading from the SOL to the core, the fluctuations in the core also become more comparable in magnitude and more visible after saturation in figures 4(*c*) and (*d*).

The results of the simulation depicted by figure 4 are quantitatively shown in the toroidal wavenumber spectrum in figure 5. The spectrum from simulation is calculated from

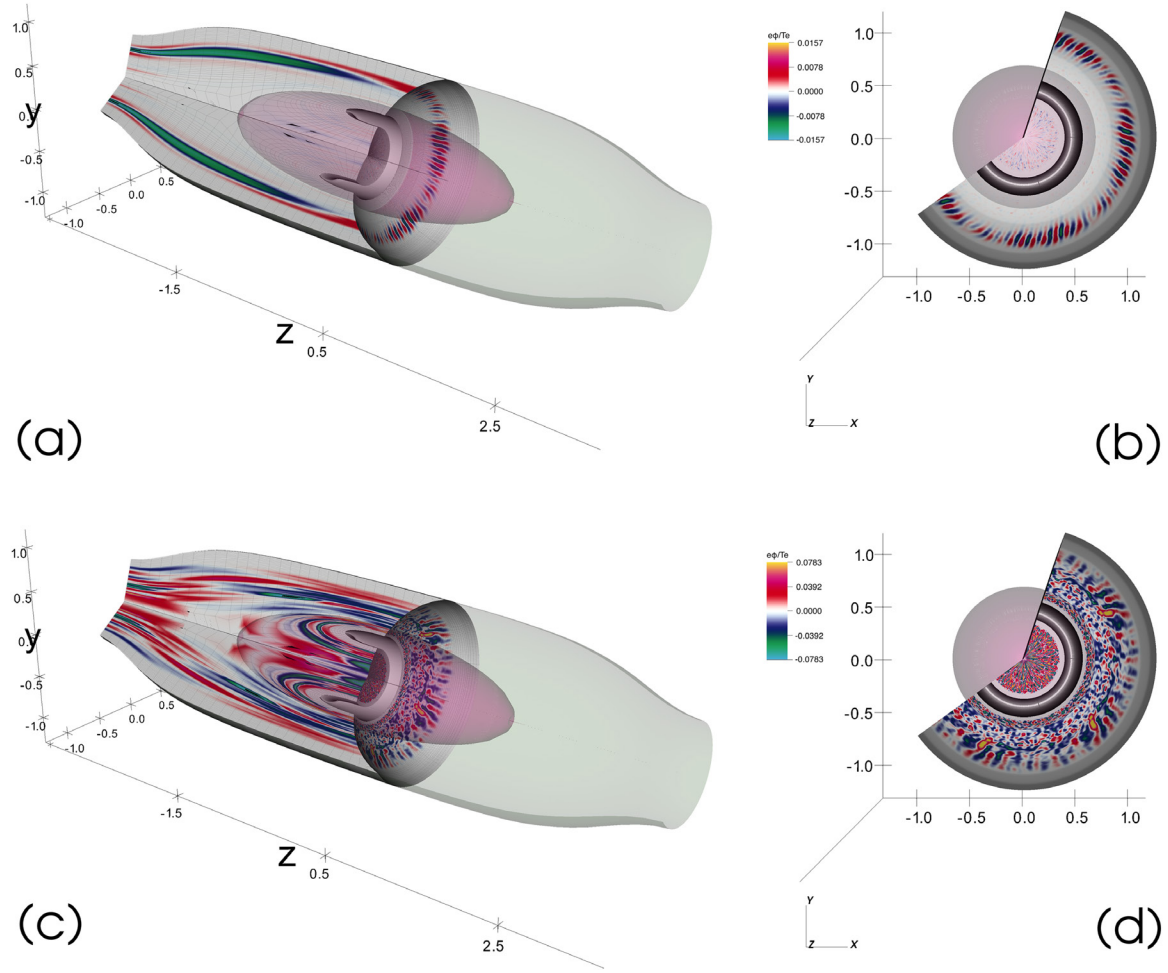

Figure 4. The electrostatic fluctuation $e\phi/T_e$ is shown at the exponential growing stage (*a*) and (*b*) and after saturation (*c*) and (*d*) from two different perspectives. The purple shell represents the separatrix, and the outer pale green shell represents the outer boundary of the simulation domain. In the second view (*b*) and (*d*), the dark ring indicates the magnetic null region which is excluded in the simulation domain; however, the inner and outer regions are still connected along the field-lines. This is more clearly seen in the first view (*a*) and (*c*) where the magnetic null region appears as the hollow section.

integrating the electrostatic potential $e\phi/T_e$ along the outer midplane at $Z = 0$ and binned according to toroidal wavenumbers (where $k_\zeta = n/R$) for a duration after saturation (between $t = 0.949$–1.03 ms). The mean simulation spectrum is plotted as the solid lines with green (red) corresponding to the spectrum calculated from the core (SOL) region. The variations over time for the spectra are plotted as the corresponding shaded regions in the figure. The quantity of the electrostatic potential is related to the density fluctuation through the Boltzmann relation (adiabatic response), $\frac{e\phi}{T_e} = \frac{\delta n_e}{n_0}$.

In comparison, the experimental measurements [10] of density fluctuations $\tilde{n}/n$ are plotted as a scatter of points in figure 5. The density fluctuation data was measured via DBS [9, 10] between 0.4–1.2 ms after plasma initiation in FRC discharges which had similar lifetimes (4–10 ms) exceeding the past FRC scalings [7]. The DBS diagnostic launches narrow Gaussian beams with different tunable frequencies and measures the backscattered signal, which is proportional to the local density fluctuation level at the resonant toroidal wavenumber. The probed wavenumber and the scattering location are calculated via GENRAY ray tracing based on reconstructed density profiles from CO2 laser interferometry and far infrared scattering.

In addition to being quantitatively comparable in normalized fluctuation levels, the shape of this fluctuation spectrum is qualitatively consistent with the experimentally measured density fluctuation spectrum. Fluctuations in the SOL are largest at long wavelengths and decrease towards shorter wavelengths due to the inverse cascade, which shifts the energy from the unstable shorter wavelength modes to the longer wavelengths. Fluctuations in the core are much lower than in the SOL due to the stabilizing influences in the core and because the fluctuations originate from outside of the core. Although core fluctuations may appear to be higher in amplitude at longer wavelengths in the simulation than shown by experiments, this is because the fluctuations in the core originate from the SOL and so the amplitude varies over time. As shown by the shaded regions in the plot, the variations over time cover a range that would fall within the experimental measurements.

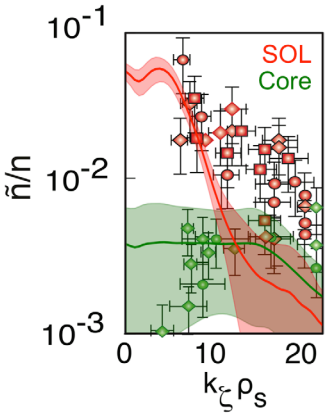

Figure 5. The fluctuation spectrum corresponding to the post-saturation time from simulation $\left(\frac{e\phi}{T_e} = \frac{\delta n_e}{n_0}\right)$ is plotted as the lines while the spectrum corresponding to the experimental measurements $\left(\frac{\delta n}{n_0}\right)$ is plotted as data points. The shaded region indicates the standard deviation of the simulation spectrum over the time period for which this data represents. The deviation over the time period is smaller for unstable longer wavelengths in the SOL where the instability is driven.

6. Conclusions

In this paper, the simulation model has been extended to include nonlinear particle effects and interaction of multiple toroidal modes in a global geometry spanning both the core and SOL regions in the FRC confinement vessel. Previous local linear simulations found linear modes to be stable in the FRC core but unstable in the SOL [11, 12, 13]. Consistent with these past simulations, linear simulations in the current work also finds instability only in the SOL region. These results are in qualitative agreement with experimental measurements of density fluctuations in the C-2/C-2U FRC plasmas, which show core fluctuations to be lower in amplitude than SOL fluctuations [10].

As shown in figure 5, with the updated global model, the current work can now go beyond qualitative comparison and directly compare with experimental measurements. Nonlinear simulations show that instability saturates at levels comparable to experimentally measured amplitudes. An inverse spectral cascade in the SOL produces a toroidal wavenumber spectrum that decreases towards shorter wavelengths. In addition, the fluctuations spread from the SOL into the core at reduced amplitudes and shorter wavelengths, which produces a core toroidal wavenumber spectrum that is much lower in amplitude at longer wavelengths. These simulated wavenumber spectra agree with the experimentally measured spectra in several features [1]: lower amplitude in the core at longer wavelengths [2], higher amplitude in the SOL at longer wavelengths [3], decreasing trend towards shorter wavelengths in the SOL.

From these fluctuations, ion energy flux across field-lines, $\Phi_{q,s} \equiv \int dv^3 \left(\frac{1}{2}mv^2 - \frac{3}{2}T_s\right)\left(\vec{v}_{\delta E\times B}\cdot\hat{\psi}\right)\delta f_s$, is calculated, which tracks the energy moving in the direction across the field-lines due to the $\delta\vec{E}\times\vec{B}$ drift from the self-consistent electric fields. Ion conductivity can then be found through Fick's law $\chi_s = \Phi_{q,s}/n_s\nabla T_s$. In the simulations of the current work, the peak ion energy flux, $\Phi_{q,\mathrm{i,max}} \sim 6\,(\mathrm{kW\,m^{-2}})$, and conductivity, $\chi_{\mathrm{i,max}} \sim 5\,(\mathrm{m^2\,s^{-1}})$, are found in the SOL. Under the adiabatic electron response model, particle flux across field-lines does not occur. However, test electron diagnostics (simulation particles which sample the self-consistent fields but do not contribute to them) have also been used to calculate an upper bound on electron transport quantities resulting in upper bound peak electron energy flux, $\Phi_{q,\mathrm{e,max}} \sim 7\,(\mathrm{MW\,m^{-2}})$, and conductivity, $\chi_{\mathrm{e,max}} \sim 0.015\,(\mathrm{m^2\,\mu s^{-1}})$.

From the upper bounds found for electron conductivity, 'worst case' estimates of energy confinement times can be estimated for the core, $\tau_{E,e} \gtrsim 75\,(\mu s)$, and SOL, $\tau_{E,e} \gtrsim 20\,(\mu s)$ (using the relation $\chi_e \approx a^2/\tau_{E,e}$, where $a \to R$ at peak values in the respective regions) comparable to experimental measurements of $\tau_{E,e} \sim 200\,(\mu s)$. Future experiments are expected to reach higher temperatures along with stronger magnetic field such that the motion of particles perpendicular to the field-lines should not change much. However, the motion of particles along the field-lines will be faster as temperature rises, which can enhance the stabilizing effect of large $k_\parallel v_\parallel$ seen in past local simulations [13]. Interestingly, in the simulations using the test electron diagnostics, electron thermal transport was found to decrease with increasing electron temperature, possibly due to the effective averaging over fluctuations in the parallel direction due the faster motion along field-lines. More conclusive results on thermal transport will require simulations with electrons which contribute to the fields as the nature of the instability may change.

Because long wavelength modes drive larger transport for the same amplitude of electric field, the wavenumber spectrum found in experiments and simulations is favourable for confinement in the FRC core. The work of the paper has shown that this spectrum arises from SOL fluctuation spreading and not from inherent core instabilities. Because the core is stable to electrostatic drift-instabilities [13] due to the effects of typical FRC features (magnetic well, short electron field-line transit along, and large FLR), core turbulence in future devices or different equilibria is also likely to originate from outside instabilities, and the fluctuation spectrum is expected to remain favourable for confinement. Low-frequency instabilities of interest which may exist in the SOL include the universal drift and ion-cyclotron electron drift modes suggested by Carlson [26] and the trapped electron mode seen in our previous local linear work.

Although the current work has extended previous simulation models, there are important physics present in experiment which have not been included. In previous local linear simulations, a drift-kinetic electron model was used and allowed for a trapped electron mode to arise in the SOL. Because these global FRC simulations are the first cross-separatrix FRC turbulence simulations that the authors know of, a simpler model using an adiabatic electron response was employed to begin. This may explain the discrepancy in the simulated SOL wavenumber spectrum, which shows slightly longer wavelengths than experiments. In upcoming work, the electron model will be extended to drift-kinetic electrons to allow for

such a trapped electron mode to arise. In addition equilibrium sheared flows are experimentally present but have not been included in this work. These sheared flows can modify the properties of linear instabilities and nonlinear turbulent structures. Future work will also include and quantify the effects of equilibrium sheared flows.

Acknowledgments

The authors would like to thank the TAE team at TAE Technologies, Inc., for equilibrium data as well as ongoing insights and collaboration in the development of these simulations. Portions of this work were carried out at University of California, Irvine with the support of the Norman Rostoker Fellowship and a TAE Grant No. TAE-200441. Simulations used the resources of DOE Office of Science User Facilities: National Energy Research Scientific Computing Center (DOE Contract No. DE-AC02-05CH11231) and Innovative and Novel Computational Impact on Theory and Experiment (INCITE) program at Argonne Leadership Computing Facility at Argonne National Laboratory (DOE Contract No. DE-AC02-06CH11357).

ORCID iDs

C.K. Lau https://orcid.org/0000-0001-6702-1461

References

[1] Tuszewski M. 1988 *Nucl. Fusion* **28** 2033
[2] Steinhauer L.C. 2011 *Phys. Plasmas* **18** 070501
[3] Chen L., Chance M.S. and Cheng C.Z. 1980 *Nucl. Fusion* **20** 901
[4] Cheng C. and Chen L. 1980 *Phys. Fluids* **23** 2242
[5] Guo H.Y. *et al* 2015 *Nat. Commun.* **6** 6897
[6] Tuszewski M. *et al* 2012 *Phys. Plasmas* **19** 056108
[7] Binderbauer M.W. *et al* 2015 *Phys. Plasmas* **22** 056110
[8] Binderbauer M.W. *et al* 2016 *AIP Conf. Proc.* **1721** 030003
[9] Schmitz L. *et al* 2014 *Rev. Sci. Instrum.* **85** 11D840
[10] Schmitz L. *et al* 2016 *Nat. Commun.* **7** 13860
[11] Fulton D.P., Lau C.K., Holod I., Lin Z. and Dettrick S. 2016 *Phys. Plasmas* **23** 012509
[12] Fulton D.P., Lau C.K., Schmitz L., Holod I., Lin Z., Tajima T., Binderbauer M.W. and The TAE Team 2016 *Phys. Plasmas* **23** 056111
[13] Lau C.K., Fulton D.P., Holod I., Lin Z., Binderbauer M., Tajima T. and Schmitz L. 2017 *Phys. Plasmas* **24** 082512
[14] Lin Z., Hahm T.S., Lee W.W., Tang W.M. and White R.B. 1998 *Science* **281** 1835–7
[15] Rosenbluth M., Krall N. and Rostoker N. 1962 Finite Larmor radius stabilization of "weakly" unstable confined plasmas (General Dynamics Corp., San Diego, CA.) (https://www.osti.gov/biblio/4808729)
[16] Gupta S. *et al* 2016 *Phys. Plasmas* **23** 052307
[17] Onofri M., Yushmanov P., Dettrick S., Barnes D., Hubbard K. and Tajima T. 2017 *Phys. Plasmas* **24** 092518
[18] Fulton D.P. 2015 Kinetic simulation of edge instability in fusion plasmas *UC Irvine Doctoral Dissertation* (https://escholarship.org/uc/item/6686z6fg)
[19] Lau C.K. 2017 Electrostatic turbulence and transport in the field-reversed configuration *UC Irvine Doctoral Dissertation* (https://escholarship.org/uc/item/56x201gs)
[20] Tajima T. 1989 *Computational Plasma Physics: With Applications to Fusion and Astrophysics* (Redwood City, CA: Addison-Wesley)
[21] Dimits A.M. and Lee W.W. 1993 *J. Comput. Phys.* **107** 2
[22] Parker S.E. and Lee W.W. 1993 *Phys. Fluids* B **5** 77
[23] Lin Z., Nishimura Y., Xiao Y., Holod I., Zhang W.L. and Chen L. 2007 *Plasma Phys. Control. Fusion* **49** 163
[24] Holod I., Zhang W.L., Xiao Y. and Lin Z. 2009 *Phys. Plasmas* **16** 122307
[25] Galeotti L., Barnes D.C., Ceccherini F. and Pegoraro F. 2011 *Phys. Plasmas* **18** 082509
[26] Carlson A.W. 1987 *Phys. Fluids* **30** 1497